

# Study on Flow Structures due to a Dimple in Channel Flow by Direct Numerical Simulation

Ming-Wei Ge, Chun-Xiao Xu and Gui-Xiang Cui

School of Aerospace Engineering, Tsinghua University, Beijing 100084, P.R China

[Received date 3/11/2012; Accepted date 10/31/2012]

## ABSTRACT

Direct numerical simulation is performed to the flows in a channel with a cosine-shaped dimple on the lower wall. Flow structures due to the dimple are studied at eight different Reynolds numbers ranging from 50 to 3000, corresponding to laminar, transitional and turbulent flows. The instability is triggered at Reynolds number around 1000. As Reynolds number increases, the separation region in the cavity of the dimple becomes big, and the pressure on the rear part of the cavity increases, resulting in the enhancement of the pressure drag. At the transitional Reynolds number, the instantaneous flow field exhibits an apparent periodic character, and the three different flow patterns are found at the three different characteristic frequencies, respectively.

## 1. INTRODUCTION

A variety of techniques used to enhance heat transfer and mixing of materials, for example, pin fins, dimpled surfaces, surfaces with protrusions, ribbed turbulators, swirl chambers, and surface roughness are reviewed by Ligrani [1]. Among these techniques, dimpled surfaces show about the same performance as the conventional ribs and pins while the increase of total drag is lower. In recent years, surfaces imprinted with dimples are studied extensively by a lot of researchers through both experiment measurement and numerical simulation. However, we still lack of consensus knowledge on the flow structures associated with the dimpled surface, especially the secondary flow and its unsteadiness which play a critical role in practical application of this technique.

The flow in a channel with dimpled walls depends on the following parameters: the maximum depth ( $h$ ) and the print diameter ( $D$ ) of the dimple, the channel half width ( $H$ ), the bulk mean velocity ( $U$ ) and the kinematic viscosity of the fluid ( $\nu$ ). For the incompressible fluid considered in the present study, the density  $\rho$  is considered as a known constant. According to the dimensional analysis, the flow is determined by three independent dimensionless parameters, which can be selected as the ratio of the dimple print diameter to the channel half width  $D^* = D/H$ , the ratio of the dimple depth to the diameter  $\varepsilon = h/D$  and the Reynolds number  $Re = UH/\nu$ .

The influence of  $D^*$  on the flow structures in the dimpled channel flow has been studied by Ligrani [2] and Mahmood [3] experimentally at  $\varepsilon = 0.2$ . They identified a primary vortex pair which is periodically shed from the central portion of each spherical dimple, and two additional secondary vortex pairs which form near the spanwise edges of each dimple. Their results show that the strength of the primary and the secondary vortex pairs increase with  $D^*$ . Won [4] experimentally studied the effects of  $\varepsilon$  on flow structures over a dimpled wall in a rectangular channel. As  $\varepsilon$  increases, the produced vortices become bigger and stronger and the turbulent transport capability is enhanced. They also found that the non-dimensionalized ejection frequency of the primary vortex pair, and the oscillating frequency of the edge vortex pair both decrease with Reynolds number, regardless of what  $\varepsilon$  is.

Various numerical simulations have been conducted to the flows over dimpled surfaces. Wang [5] performed simulation to the laminar flow and found the "horse-shoe vortex" inside a single dimple. A realizable  $k-\varepsilon$  turbulence model was used by Park [6, 7] and Won [8] to predict the fully turbulent air flow in a channel with deep dimples. The centrally located primary vortex pair and the edge-located secondary vortex pair have been caught successfully in their steady RANS (Reynolds Averaged Navier

Stokes) simulations, but the unsteadiness of the flow structures failed to be grasped. Wang [9] and Elyyan [10, 11] performed direct and large eddy simulations to the flow over the surface with dimple arrays, and mainly focused on the changes in the turbulence statistics and the enhancement of heat transfer, respectively.

In the present study, our main concern is the influence of the Reynolds number on the flow structures due to a single dimple. Hence the dimple with fixed  $D^*$  and  $\varepsilon$  is employed and is placed on the lower wall of a plane channel. The direct numerical simulations at different  $Re$  are performed, covering the range of laminar, transitional and turbulent flow regimes, to obtain a systematic knowledge about the influence of Reynolds numbers on flow structures due to a dimple.

## 2. NUMERICAL METHOD

The flow of incompressible Newtonian fluid in a channel with dimpled walls is governed by the Navier-Stokes equations and the continuity equation. The equations non-dimensionalized by the bulk mean velocity  $U$  and the channel half width  $H$  are

$$\frac{\partial u_i}{\partial t} + u_j \frac{\partial u_i}{\partial x_j} = -\frac{\partial p}{\partial x_i} + \frac{1}{Re} \frac{\partial^2 u_i}{\partial x_j \partial x_j}, \quad (1)$$

$$\frac{\partial u_i}{\partial x_i} = 0. \quad (2)$$

In the streamwise ( $x$  or  $x_1$ ) and spanwise ( $z$  or  $x_3$ ) directions, the flow is assumed periodic. In the vertical direction ( $y$  or  $x_2$ ), the no-slip condition is used at the walls.

The locations of the upper and lower walls can be represented by  $y = 1 + \eta_u$  and  $y = -1 + \eta_d$ , respectively. Here  $\eta_u$  and  $\eta_d$  represent the amount of the deformation of the corresponding walls. The computational coordinate system  $\xi_i$  is defined so as to

$$x_1 = \xi_1, \quad x_2 = \xi_2(1 + \eta) + \eta_0, \quad x_3 = \xi_3 \quad (3)$$

in which  $\eta = (\eta_u - \eta_d)/2$ , and  $\eta_0 = (\eta_u + \eta_d)/2$ . In the computational space, the upper and lower walls are located at  $\xi_2 = 1$  and  $\xi_2 = -1$ , and the velocity conditions at the walls can be written as

$$\xi_2 = -1: \quad u = 0, \quad v = 0, \quad w = 0 \quad (4)$$

$$\xi_2 = 1: \quad u = 0, \quad v = 0, \quad w = 0 \quad (5)$$

By the above coordinate transform, the spatial derivatives can be represented by

$$\frac{\partial}{\partial x_i} = \frac{\partial}{\partial \xi_i} + \phi_i \frac{\partial}{\partial \xi_2} \quad (6)$$

in which  $\phi_i = \varphi_i - \delta_{i2}$ , and

$$\varphi_i = \frac{\partial \xi_2}{\partial x_i} = \begin{cases} -\frac{1}{1 + \eta} \left( \xi_2 \frac{\partial \eta}{\partial \xi_i} + \frac{\partial \eta_0}{\partial \xi_i} \right), & i = 1, 3 \\ \frac{1}{1 + \eta}, & i = 2 \end{cases} \quad (7)$$

The flow quantities in computational space are represented by the expansions of Fourier series and Chebyshev polynomials. Hence for spatial discretization of the governing equations, Fourier-Galerkin method is used in the streamwise and spanwise directions, and Chebyshev-Tau method is adopted in the wall-normal direction. The extra terms due to the coordinate transform are iterated by a modified

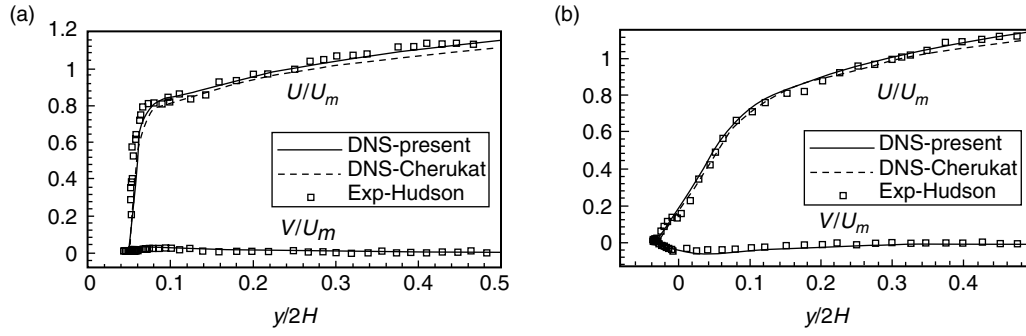


Figure 1. Distribution of mean velocity at (a) crest and (b) trough locations.

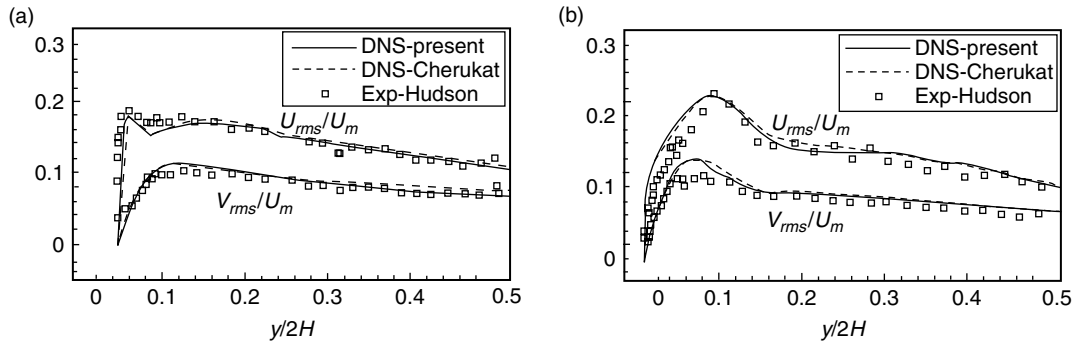


Figure 2. Root-mean square of velocity fluctuations at (a) crest and (b) trough locations.

Newtonian iteration method. The third-order time-splitting method is employed for time advancement. For more details see Ge [12].

The turbulent channel flow with a static wavy wall is first simulated and compared with the experimental measurements by Hudson [13] and DNS results by Cherukat [14] to validate the code. The lower wall is set to be sinusoidal in streamwise direction, and the upper wall is flat, i.e.

$$\eta_u = 1, \quad \eta_d = a \sin(2\pi x / \lambda) \tag{8}$$

In our simulation, the amplitude of wall deformation is chosen to be  $a = 0.1$ , and the wave length is  $\lambda = 2$ , which is in accordance with Hudson’s experiments. The Reynolds number based on bulk mean velocity and channel half width is set to be 3380 to match the experiments. The size of the computational domain is  $8 \times 2 \times 4$  in the streamwise, vertical and spanwise directions, respectively, and  $64 \times 65 \times 64$  grids are used accordingly.

The distributions of the mean velocity and the root-mean square of the velocity fluctuations along the vertical direction at two different streamwise locations (crest and trough) are shown in Fig. 1 and Fig. 2. Hudson’s [13] experimental and Cherukat’s [14] numerical results are also shown for comparison. The present results are very similar to Cherukat’s numerical results, and they are all in good agreement with Hudson’s experimental measurements.

### 3. RESULTS AND DISCUSSION

#### 3.1. Computation Settings

A cosine-shaped dimple is imposed at the centre of the lower wall with  $D/H = 1.0$  and  $h/D = 0.2$  while the upper wall is smooth (see Fig 3). The dimple profile can be described by

$$\eta_d(x, z, t) = \begin{cases} -\frac{h}{2} \left( 1 + \cos \frac{2\pi r}{D} \right), & r < \frac{D}{2} \\ 0, & r \geq \frac{D}{2} \end{cases} \tag{9}$$

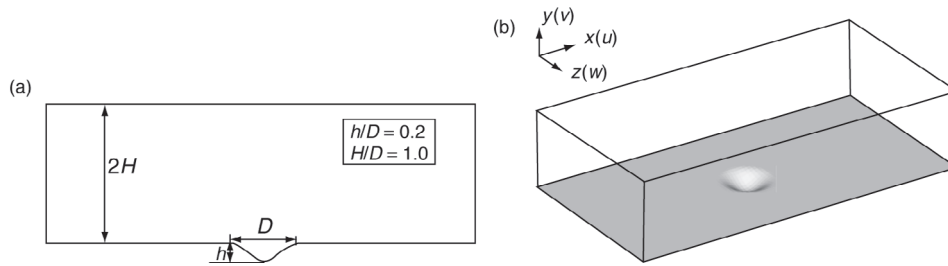


Figure 3. Computational domain and coordinate system. (a) Vertical plane through dimple centre and (b) global view.

where  $r = [(x - x_0)^2 + (z - z_0)^2]^{1/2}$ ,  $(x_0, z_0)$  is the centre of the dimple at the plane of the channel floor. The computational domain is  $2\pi \times 2 \times \pi$  in the  $x$ ,  $y$ , and  $z$  directions. The simulations are starting from the laminar plane Poiseuille flow, and the flow rates are kept constant during the development of the flow by adjusting the driving pressure gradient every time step according to the friction and pressure drag.

Eight cases at different Reynolds numbers ranging from  $Re = 50$  to 3000 have been simulated. The grids of  $64 \times 65 \times 32$  are used in the cases of lower Reynolds numbers ranging from 50 to 1700, and higher resolution in vertical direction with  $64 \times 129 \times 64$  grids are adopted for the higher Reynolds number flows.

### 3.2. Laminar Flow

For the Reynolds number ranging from 50 to 750, the flows keep laminar. In the following, the flow structures and the drag due to the dimple in this laminar flow regime will be shown at  $Re = 50$ , 250, 500 and 750.

The second invariant of velocity gradient tensor,  $Q = (\|\Omega\|^2 - \|\mathbf{S}\|^2)/2$ , is a widely used flow quantity to show vortical structures, in which  $\Omega$  is the rotation tensor, and  $\mathbf{S}$  is the tensor of strain rate [15]. In the region of  $Q > 0$ , the rotation dominates over the strain rate, and hence the iso-surfaces of positive  $Q$  can be used to identify and visualize the strong vortical structures. Fig. 4 shows the iso-surface of  $Q = 0.2$ . Arc structures are generated at the leading and rear edge of the dimple, where the flow is entering and leaving the dimple cavity. Fig. 4 indicates that the intensity of the arc structures becomes weaker with the increase of the Reynolds number. In order to reveal the structures more clearly, the streamlines in the vertical plane ( $x$ - $z$ ) across the centre of the dimple are shown in Fig 5. At the lowest Reynolds number,  $Re = 50$ , no flow separation and recirculation can be observed in the dimple cavity.

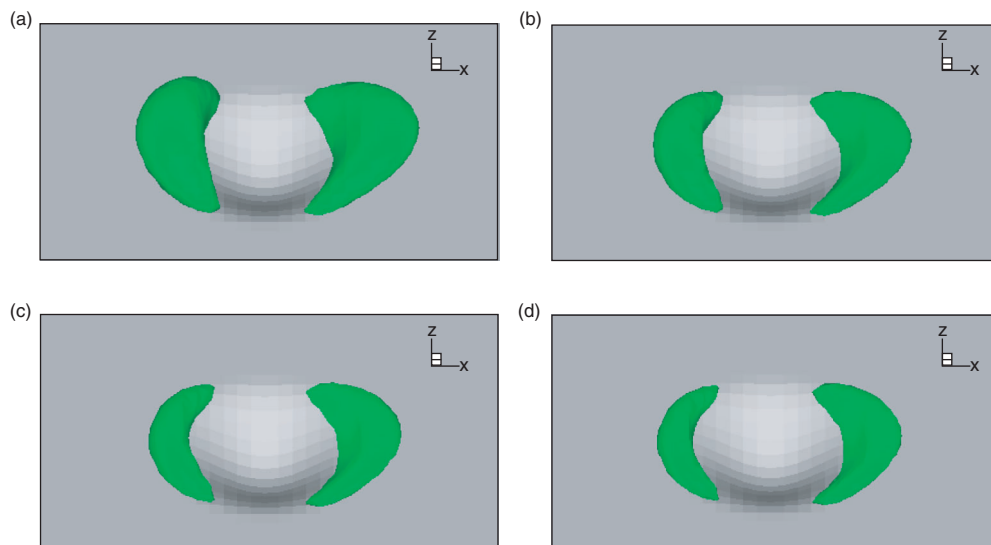


Figure 4. Flow structures shown by iso-surfaces of  $Q = 0.2$  for (a)  $Re = 50$ , (b)  $Re = 250$ , (c)  $Re = 500$  and (d)  $Re = 750$ .

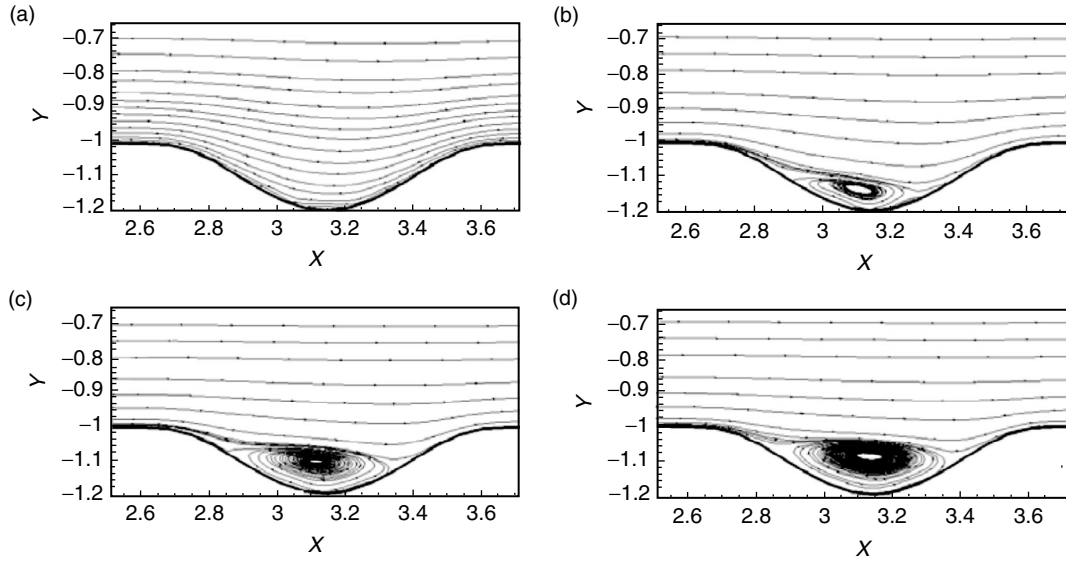


Figure 5. Streamlines in  $(x-y)$  plane across dimple centre at (a)  $Re = 50$ , (b)  $Re = 250$ , (c)  $Re = 500$  and (d)  $Re = 750$ .

However, with the increase of the Reynolds number, the flow starts to separate at the leading edge of the dimple. The shear layer in the separation region is drawn into the dimple cavity by the vortex and then reattaches downstream. The intensity of the vortex in the dimple cavity becomes stronger with the separation becomes bigger. At  $Re = 750$ , the fluids flow over the separation domain smoothly, and the edges of the dimple seems to have little influence on the main flow.

The origin of the drag at the dimpled surface is analyzed. The total drag acting on the lower wall consists of the friction drag and the pressure drag. For an element of the wall surface  $dA = \sqrt{1 + (\partial\eta_d / \partial x)^2 + (\partial\eta_d / \partial z)^2} dx dz$ , the unit vector in its normal direction is

$$\mathbf{n} = \frac{1}{\sqrt{1 + (\partial\eta_d / \partial x)^2 + (\partial\eta_d / \partial z)^2}} \left( -\frac{\partial\eta_d}{\partial x}, 1, -\frac{\partial\eta_d}{\partial z} \right)$$

The friction force and pressure force per unit projected area on  $(x, z)$ -plane are

$$f_x^f(x, z) = \frac{1}{Re} \left[ -2 \frac{\partial u}{\partial x} \frac{\partial \eta_d}{\partial x} + \left( \frac{\partial u}{\partial y} + \frac{\partial v}{\partial x} \right) - \left( \frac{\partial u}{\partial z} + \frac{\partial w}{\partial x} \right) \frac{\partial \eta_d}{\partial z} \right] \quad (10)$$

and

$$f_x^p(x, z) = p \frac{\partial \eta_d}{\partial x} \quad (11)$$

The averaged pressure on the upper flat wall is set to be zero.  $\left[ (f_x^f)_{dimple} - (\bar{f}_x^f)_{flat} \right] / (\bar{f}_x^f)_{flat}$  and  $(f_x^p)_{dimple} / (\bar{f}_x^f)_{flat}$  are used to characterize the influence of the dimple on the friction force and pressure force. Here  $(f_x^f)_{dimple}$  and  $(f_x^p)_{dimple}$  represent the friction and pressure drag per unit area on the dimpled lower wall, and  $(\bar{f}_x^f)_{flat}$ , which is taken as a reference in the present study, is the averaged friction drag in a flat channel at the same Reynolds number.

Contours of  $\left[ (f_x^f)_{dimple} - (\bar{f}_x^f)_{flat} \right] / (\bar{f}_x^f)_{flat}$  are shown in the Fig 6. The region with reduced friction drag almost occupies the whole dimple cavity, and those with enhanced friction appear near the leading

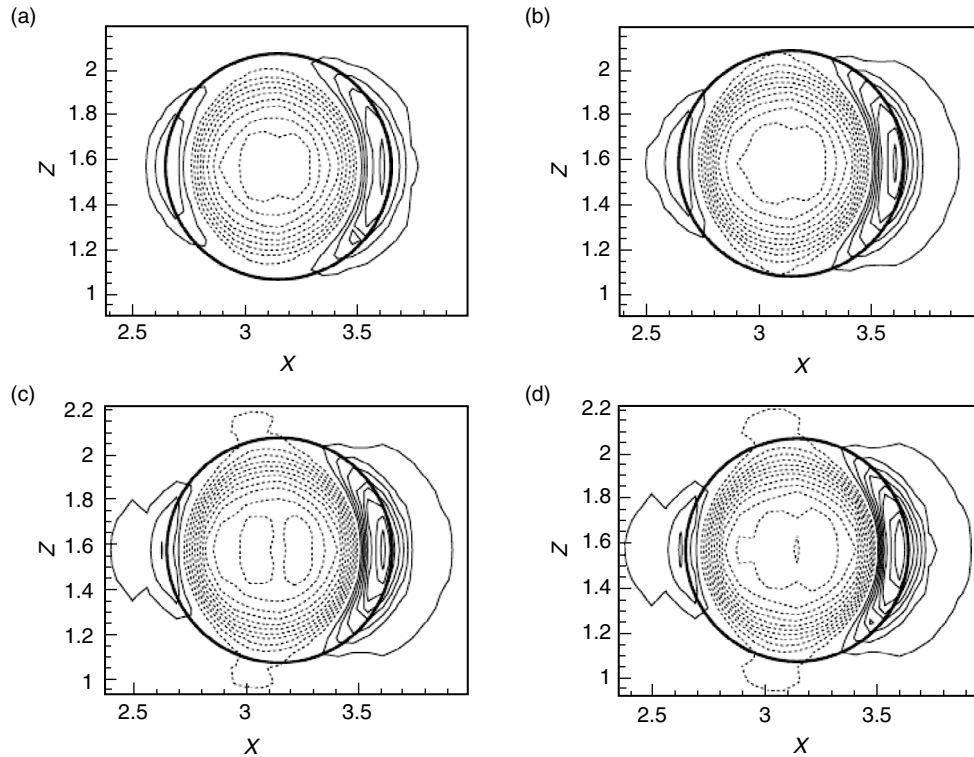


Figure 6. Contours of  $\left[ \left( f_x^f \right)_{dimple} - \left( \bar{f}_x^f \right)_{flat} \right] / \left( \bar{f}_x^f \right)_{flat}$  for (a)  $Re = 50$ , (b)  $Re = 250$ , (c)  $Re = 500$  and (d)  $Re = 750$ . Dashed lines represent negative values. Contour intervals are 0.1.

and rear edge of the dimple. The density of the contour lines increases with Reynolds number in both the lower and the higher friction regions, indicating that with the increase in  $Re$ , the friction reduction in dimple cavity and enhancement near dimple edges are both amplified. The influence of the side edges to the friction drag is not significant.

Contours of  $\left( f_x^p \right)_{dimple} / \left( \bar{f}_x^f \right)_{flat}$  are shown in Fig 7. At  $Re = 50$ , the positive and negative pressure drag per unit area reveals an upstream-downstream symmetrical distribution relative to the dimple centre, and hence the averaged pressure drag is small, as shown in Fig. 8. As the Reynolds number increases, the pressure drag in the left positive region is intensified, while that in the right negative region is attenuated, resulting in the increase of the averaged pressure drag, as seen in Fig. 8. At  $Re = 750$ , the positive pressure drag even appears in the right negative region of the dimple cavity.

The ratio of the averaged pressure drag to the total drag is shown in Fig 8. It is clear that the contribution of the pressure drag to the total drag is obviously increased as the Reynolds number increases.

### 3.3. Turbulent Flow

When the Reynolds number exceeds about 1000, transition is triggered and the flow becomes turbulent. Turbulence statistics are obtained by time averaging over about 1000 instantaneous flow realizations. The mean flow structures as well as the unsteadiness of the instantaneous flow structures due to the dimple will be discussed in the following.

#### 3.3.1. Mean Flow Structures

The iso-surface of  $Q = 1.0$  are shown in Fig. 9 for the higher Reynolds number cases. Arc structures generated at the rear and front edge of the dimple are much stronger than those in the laminar flows. At  $Re = 1500$ , the vortex inside the dimple cavity becomes strong enough to be identified by the iso-surface of  $Q = 1.0$ . With the increase in Reynolds number, both the arc vortices at the rear and leading edge and that inside the cavity of the dimple becomes stronger and stronger.

Streamlines in the  $x$ - $y$  planes across the centre of the dimple are shown in Fig 10. The dimple is fully

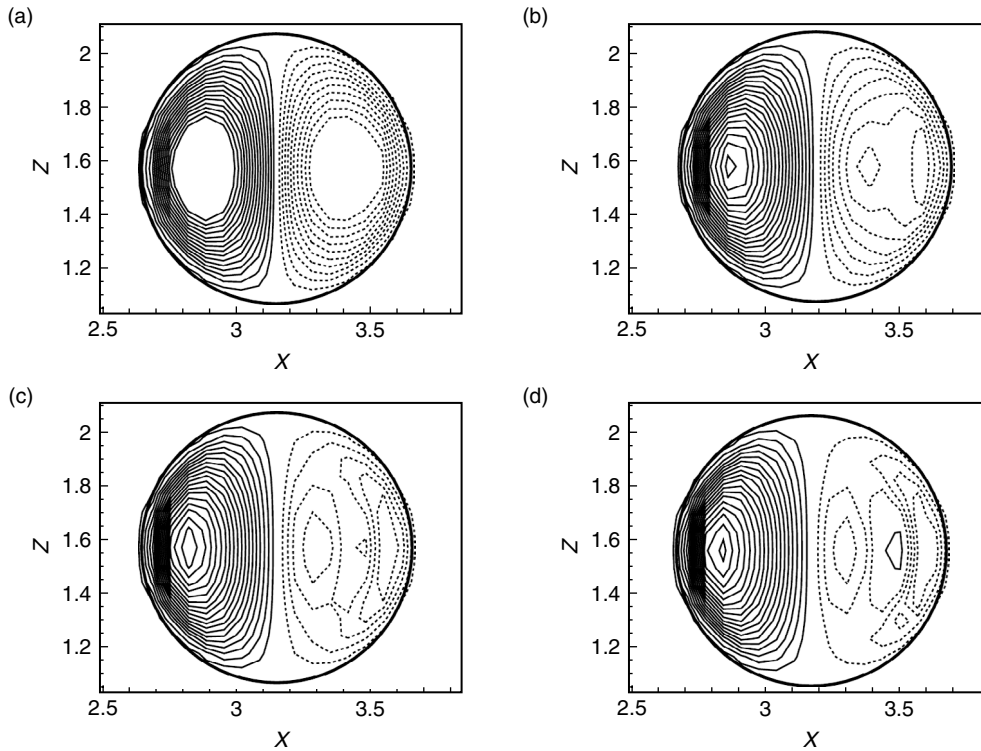


Figure 7. Contours of  $(f_x^p)_{dimple} / (\bar{f}_x^f)_{flat}$  for (a)  $Re = 50$ , (b)  $Re = 250$ , (c)  $Re = 500$  and (d)  $Re = 750$ . Dashed lines represent negative values. Contour intervals are 0.1.

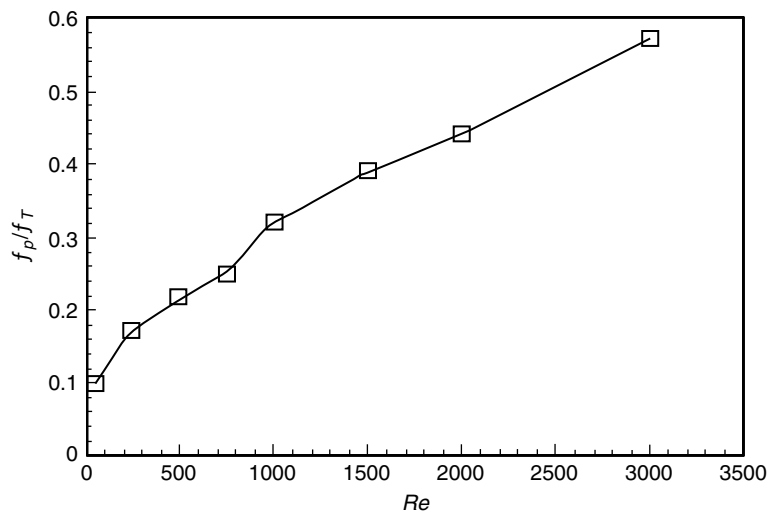


Figure 8. Ratio of pressure drag to total drag at different Reynolds numbers.

filled with the separation vortex. As the Reynolds number increases, the core of the vortex is gradually pushed downstream by the mean flow, and the space for the downwash flow in the dimple cavity is squeezed. Therefore the downwash flow is accelerated, causing the centre of the low friction region gradually moving to the back wall of the dimple, as can be seen in Fig 11.

Contours of  $(f_x^p)_{dimple} / (\bar{f}_x^f)_{flat}$  are shown in Fig. 12. As the Reynolds number increases, the core of the vortex inside the dimple cavity moves downstream, and a positive pressure drag region appears in the right part of the dimple cavity, which is occupied by the negative pressure drag in the laminar flow cases, as shown in Fig. 7. Therefore the pressure drag in turbulent cases is far larger than that in laminar

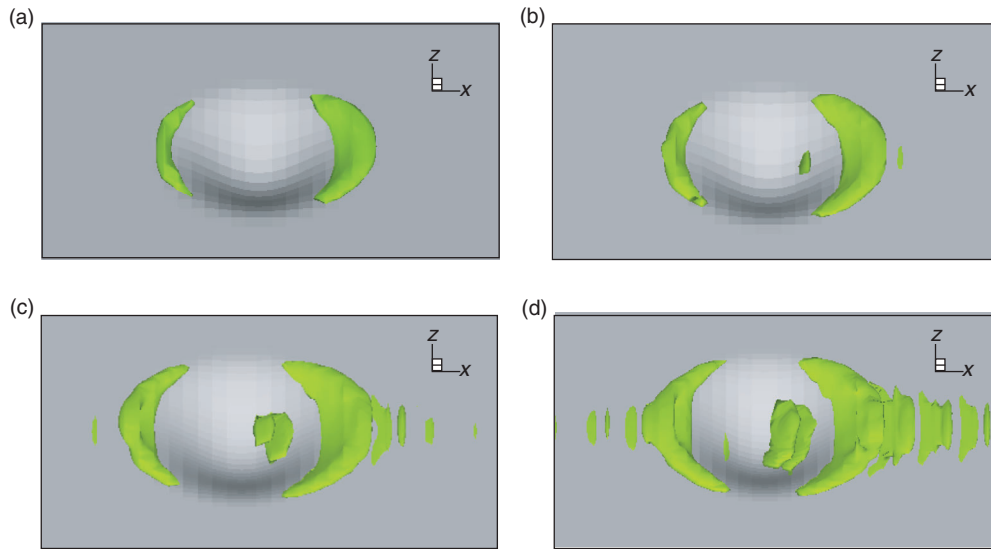


Figure 9. Flow structures shown by iso-surfaces of  $Q = 1.0$  for (a)  $Re = 1000$ , (b)  $Re = 1500$ , (c)  $Re = 2000$  and (d)  $Re = 3000$ .

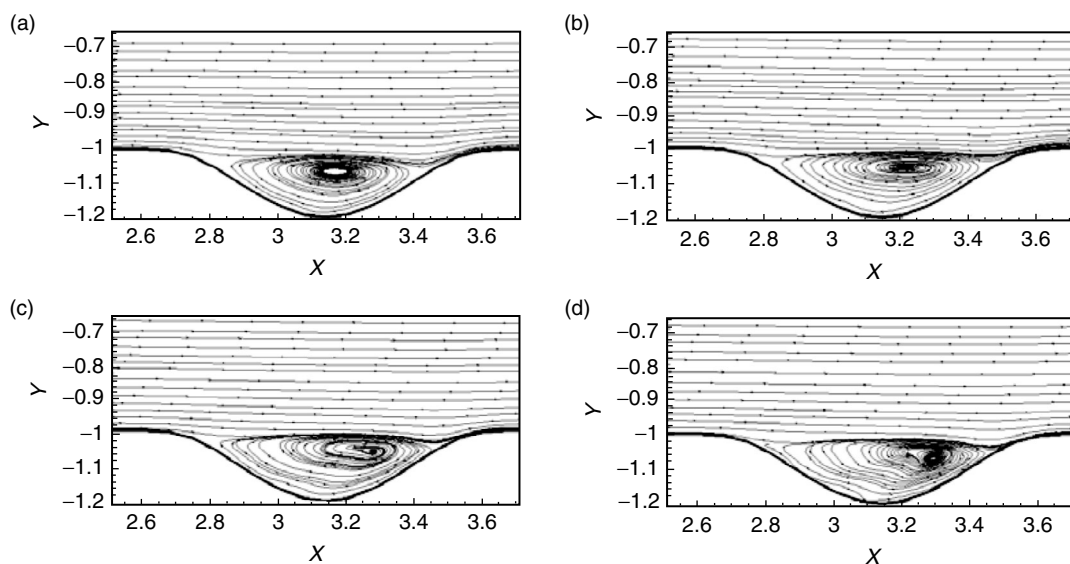


Figure 10. Streamlines in the  $x$ - $y$  plane across the dimple centre for (a)  $Re = 1000$ , (b)  $Re = 1500$ , (c)  $Re = 2000$  and (d)  $Re = 3000$ .

cases.

The ratio of the averaged pressure drag to the total drag is shown in Fig. 8 at different Reynolds numbers. It can be seen that as the Reynolds number increases, the contribution of the pressure drag to the total drag grows quickly. At  $Re = 3000$ , its proportion is even larger than 50%, indicating that at higher Reynolds numbers the pressure drag is dominant over the friction drag.

### 3.3.2. Instantaneous Flow Structures

The unsteadiness of flow structures due to dimples was studied experimentally by Ligrani et al [2]. They used the spherical dimple array with  $D^* = 2, 4$  and  $8$ , and found the continuously periodic shedding of the primary vortex pair from the central portion of each dimple at  $Re = 300\sim 5500$ . In the present study, the different unsteady flow structures have been identified at different characteristic frequencies. The unsteadiness of the flow structures will be described in the following, and the

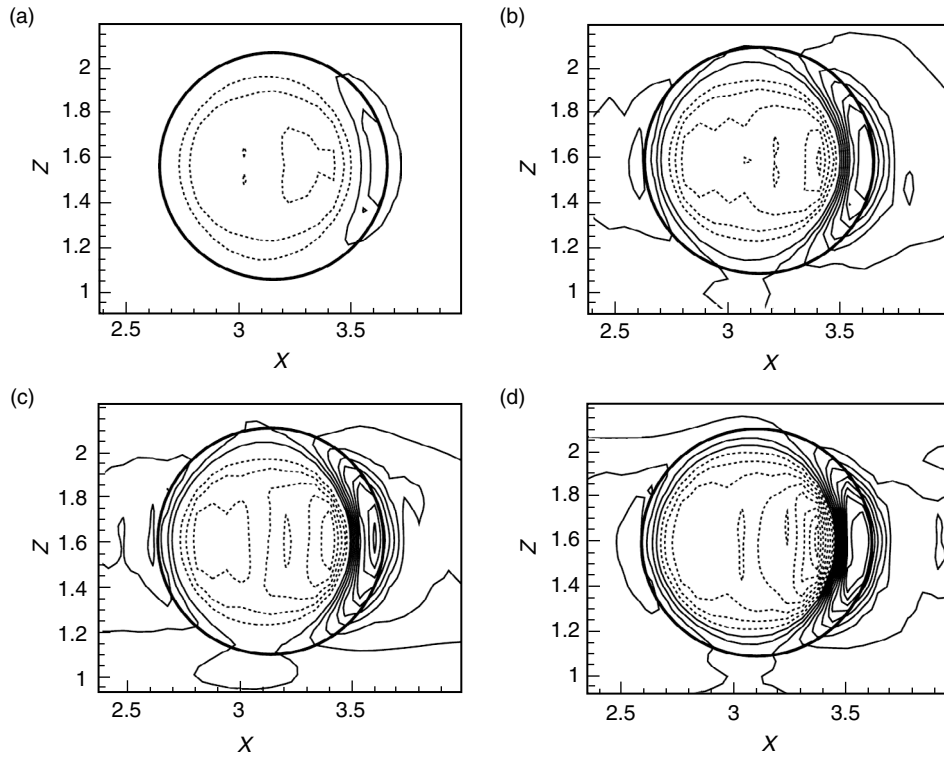


Figure 11. Contours of  $\left[ \left( f_x^f \right)_{dimple} - \left( \bar{f}_x^f \right)_{flat} \right] / \left( \bar{f}_x^f \right)_{flat}$  for (a)  $Re = 1000$ , (b)  $Re = 1500$ , (c)  $Re = 2000$  and (d)  $Re = 3000$ . Dashed lines represent negative values. Contour intervals are 0.4.

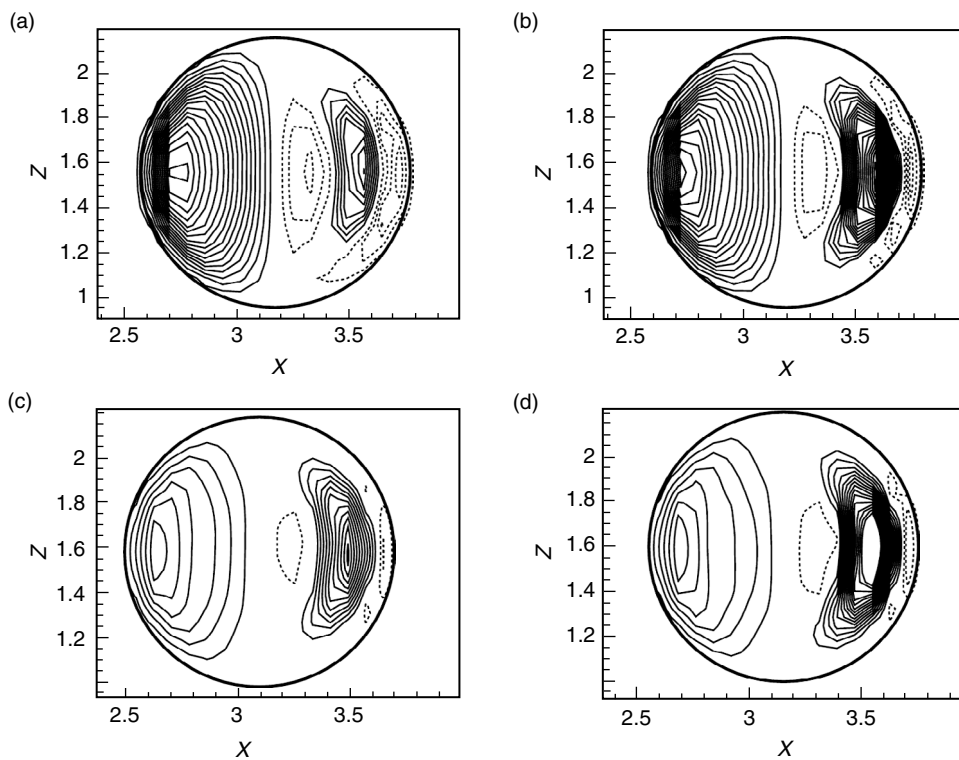


Figure 12. Contours of  $\left( f_x^p \right)_{dimple} / \left( \bar{f}_x^f \right)_{flat}$  for (a)  $Re = 1000$ , (b)  $Re = 1500$ , (c)  $Re = 2000$  and (d)  $Re = 3000$ . Dashed lines represent negative values. Contour intervals are 0.5.

Reynolds number effect will also be discussed.

A fictitious probe is put in the flow field just behind the dimple at  $\Delta x = 0.785$ ,  $\Delta y = 0.23$ , and  $\Delta z = 0$ , as shown in the insertion of Fig. 13(a). Here  $\Delta x$  and  $\Delta z$  refer to the streamwise and spanwise distance to the print centre of the dimple, and  $\Delta y$  is the distance to the wall. Fig. 13 shows the time history of the instantaneous streamwise velocity detected by the probe at Reynolds number 1000, 1500 and 3000. At  $Re = 1000$ , the instability is developed in the flow, and the streamwise velocity signal exhibits an obviously periodic characteristic. However, in the whole time range, there is not an unique dominant frequency, because the period changes with time. At  $Re = 1500$ , the signal becomes more random, and the periodic characteristic is weakened. At  $Re = 3000$ , the flow becomes fully turbulent.

The unsteady flow structures at  $Re = 1000$  is studied in more detail because of its obvious periodicity. By scrutinizing the flow signals carefully, we found that in the whole time interval between  $t = 500$  to 1000, there appears three different frequencies, namely  $f = 0.15$ , 0.31 and 0.20, corresponding

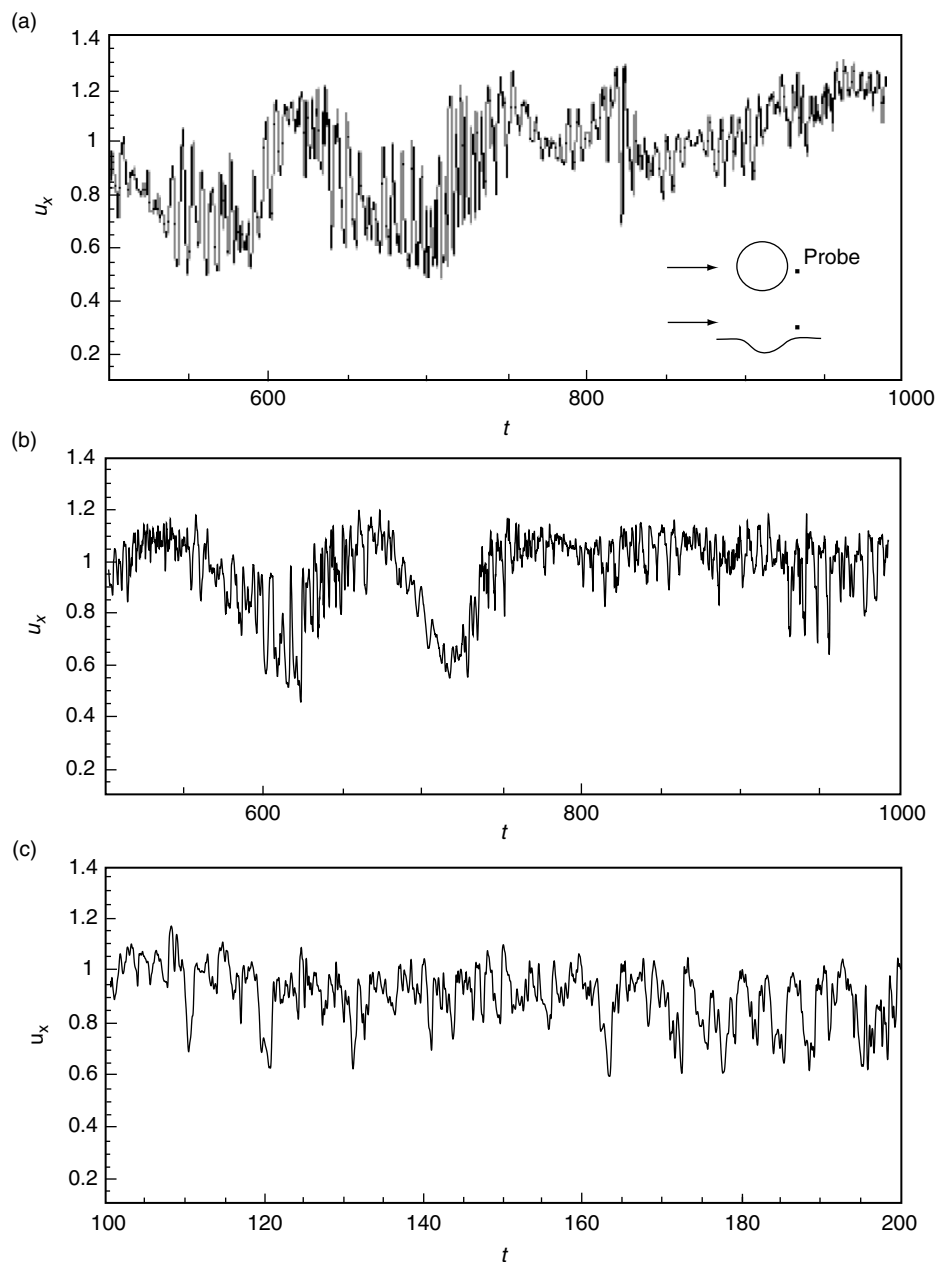


Figure 13. Instantaneous flow velocities for (a)  $Re = 1000$ , (b)  $Re = 1500$ , (c)  $Re = 3000$ .

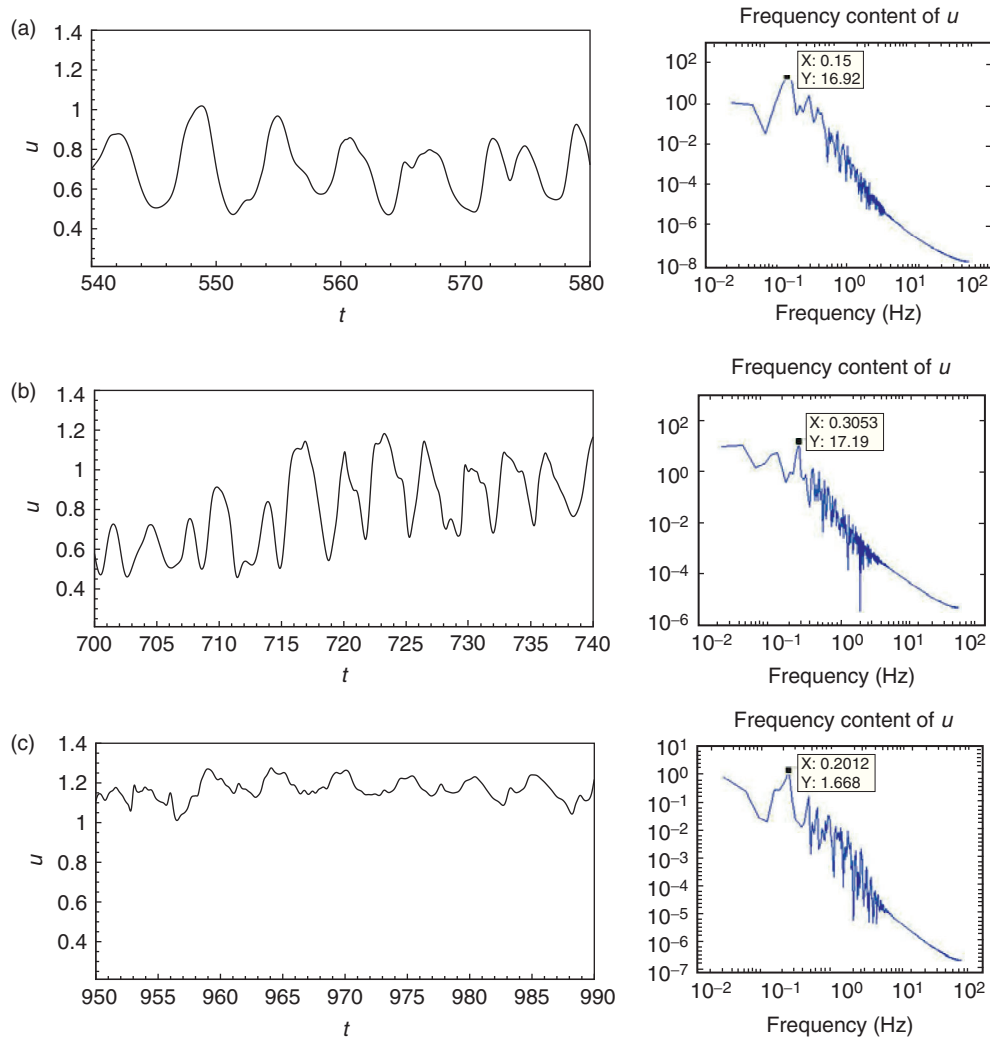


Figure 14. Time history of streamwise velocity (left) and frequency spectrum (right) at  $Re = 1000$ . (a)  $t = 540 \sim 580$ , (b)  $t = 700 \sim 740$ , (c)  $t = 950 \sim 990$ .

to the time segments of  $[540, 580]$ ,  $[700, 740]$  and  $[950, 990]$ . The time histories of the streamwise velocity in the three different time segments are shown in Fig. 14, the corresponding frequency spectra are also included in the figure. The flow patterns are described by the streamlines around the vortex core at seven different phases in one period. The vortex core is identified by the extreme negative values of  $\lambda_2$ , which is the second eigenvalue of the tensor of  $\mathbf{S}^2 + \mathbf{\Omega}^2$  [15].

During  $t = 540 \sim 580$ , the dominant frequency is  $f = 0.15$ , as shown in Fig. 14(a). The corresponding flow pattern is shown in Fig. 15. Seven different time instants are selected in a period, as indicated in the top-left figure in Fig. 15. The fluid flows into the dimple from one side of the leading edge of the dimple, and a spanwise vortex forms in the dimple cavity, which throw the injected fluid up and out of the cavity from the side edge of the dimple (Fig. 15A). As the flow develops, the head of the vortex raises and the line of the vortex core turns clockwise (Fig. 15B-E). At the same time, the vertical component of the vortex take the fluid up from the bottom of the cavity, and then the fluid is mixed with the outer flow and shed from the middle of the dimple rear edge (Fig. 15E). After that, new fluid assembles in the cavity of the dimple and a new spanwise vortex forms there (Fig. 15F-G), starting a new cycle.

During  $t = 700 \sim 740$ , the dominant frequency is  $f = 0.31$ , as shown in Fig. 14(b). The flow pattern at this frequency is shown in Fig. 16. The fluid flows into the dimple cavity from the two sides of the leading edge, a  $\Lambda$ -vortex consisting of two counter-rotating legs is formed there (Fig. 16A). The

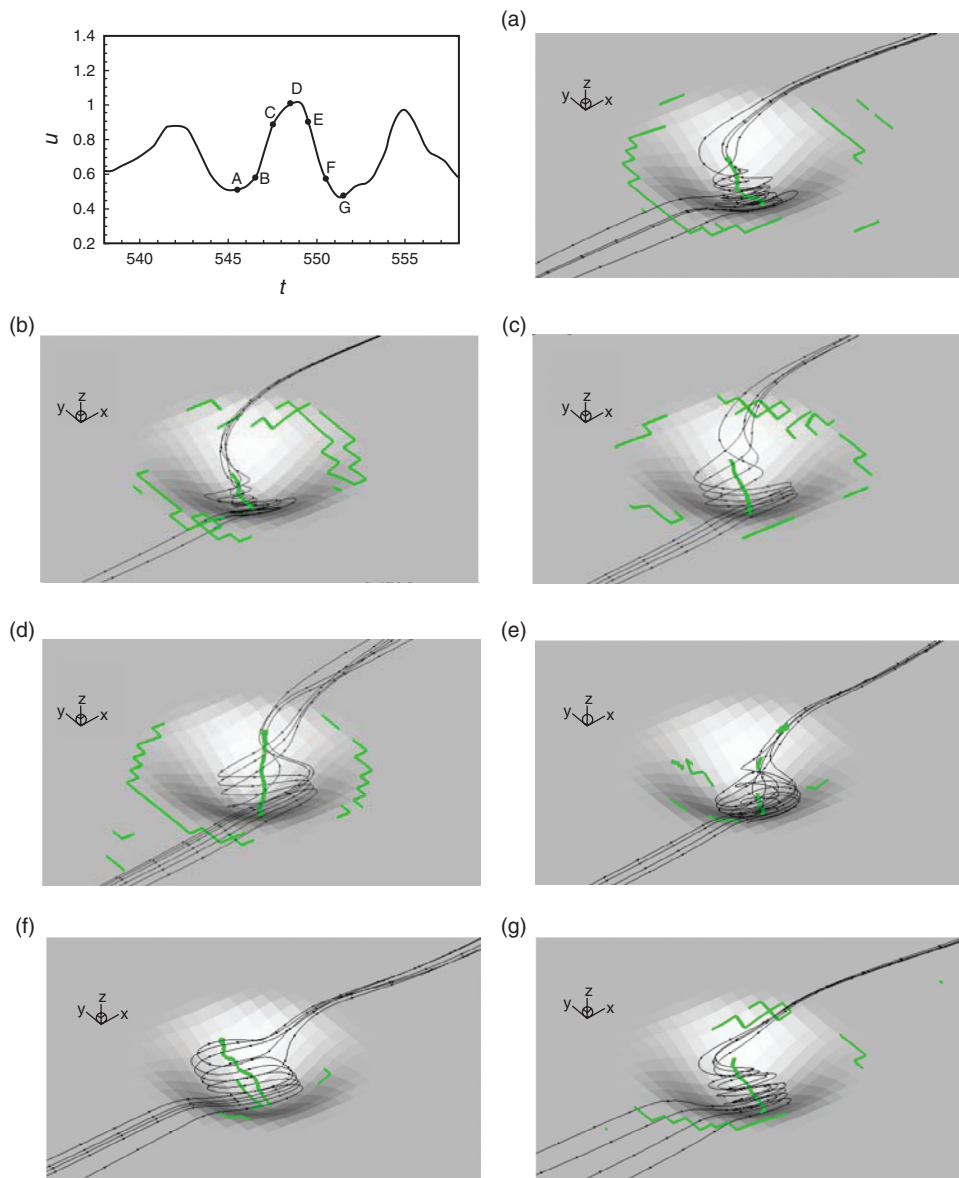


Figure 15. Streamlines and vortex cores at 7 different phases in one period corresponding to  $f = 0.15$  at  $Re = 1000$ .

$\Lambda$ -vortex throws the injected fluid out of the cavity in the middle of the rear edge of the dimple (Fig. 16A–C). As the flow develops, one of the two vortex legs (the right leg in this case) becomes weaker and weaker, and the stronger one (the left leg) begins to align in the streamwise direction and dominates the flow in the dimple cavity. The fluid is entrained into the cavity from one side of the leading edge, and is thrown out of the cavity from the other side of the rear edge (Fig. 16D–F). The imbalance between the two legs cannot last any longer. Under the influence of the outer main flow, the dominant vortex leg gradually withdraws to its former position, and a new counter-rotating vortex leg is generated and grows gradually, thus, the new  $\Lambda$ -vortex forms again (Fig. 16G).

During  $t = 950 \sim 990$ , the dominant frequency is  $f = 0.20$ , as shown in Fig. 14(c). The corresponding flow pattern at this frequency is shown in Fig. 17. It is characterized by a relatively stable spanwise vortex. With the influence of the external flow, the fluids may be entrained into the cavity from one side of the leading edge and thrown out of the cavity from the other side of the trailing edge, as shown by Fig. 17C and 17F, or get into the dimple in the middle of the leading edge and leave at the two sides of the trailing edge, see Fig. 17E. This pattern occurs later in time, and resembles the averaged flow

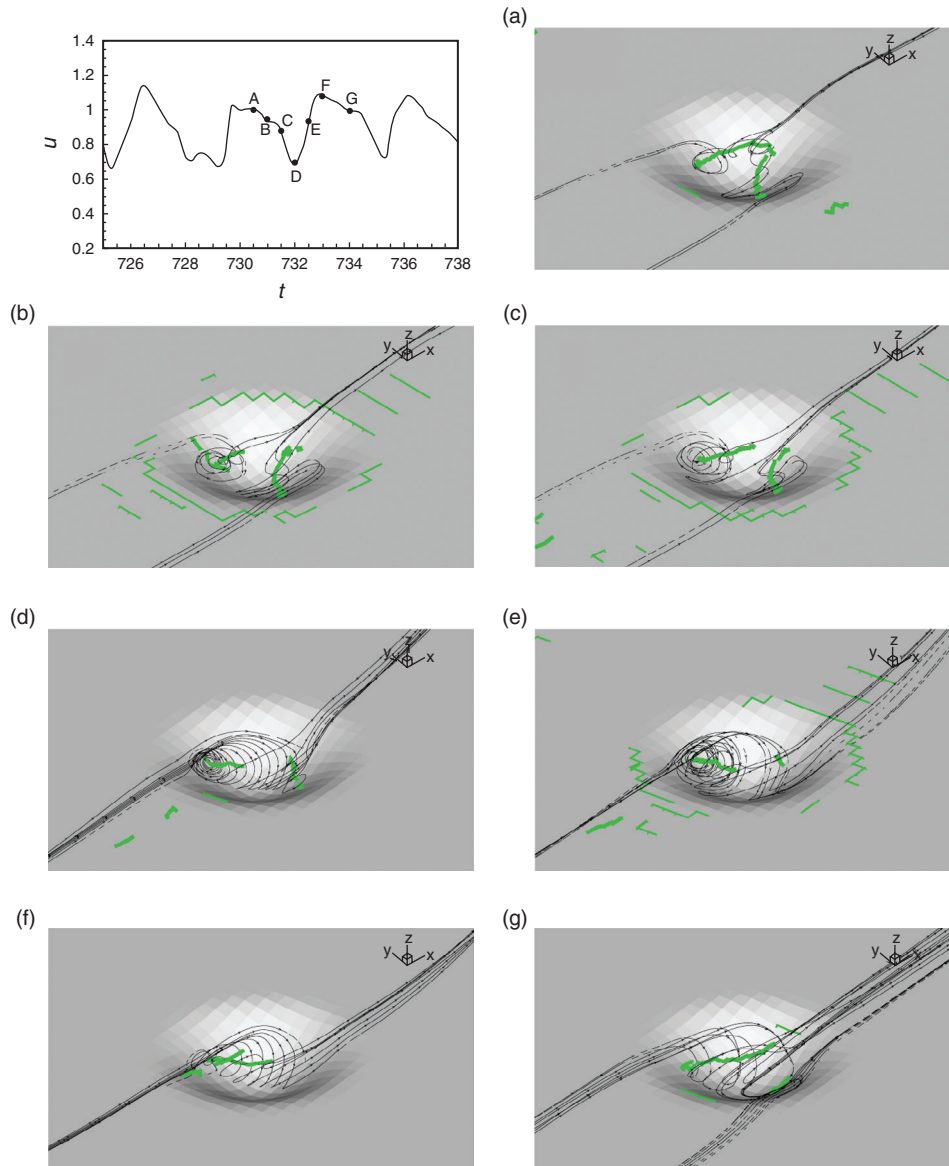


Figure 16. Streamlines and vortex cores at 7 different phases in one period corresponding to  $f = 0.31$  at  $Re = 1000$ .

structures much more than the other two patterns.

At  $Re = 1500$ , the flow becomes more complex. The three flow patterns can still be identified. However, because of the random signals of the flow field, the patterns are not as clear as those in the low Reynolds number case. As the Reynolds is increased to 3000, the flow becomes fully turbulent. The streamwise vortices shedding from the dimple cavity, similar to that described by Ligrani et al [2], can be clearly observed.

It is worth to note that the three characteristic frequencies identified in the present study is much higher than the shedding frequency of the primary vortex pair observed in Won et al [4]'s experiment. The most probable reason is that our simulation is focused on a single dimple, while their experiments were performed for a stagger-arranged dimple arrays. The print diameters are also different. In our simulation,  $D^*$  is fixed to be 1, while it is 2 in their experiments. Isaev et al [16] performed RANS simulation to a spherical dimple at a much higher Reynolds number. Although the unsteadiness cannot be predicted in their simulation, the counter-rotating streamwise vortices in dimple cavity observed in their simulation are similar to the two legs of the  $\Lambda$ -vortex identified in

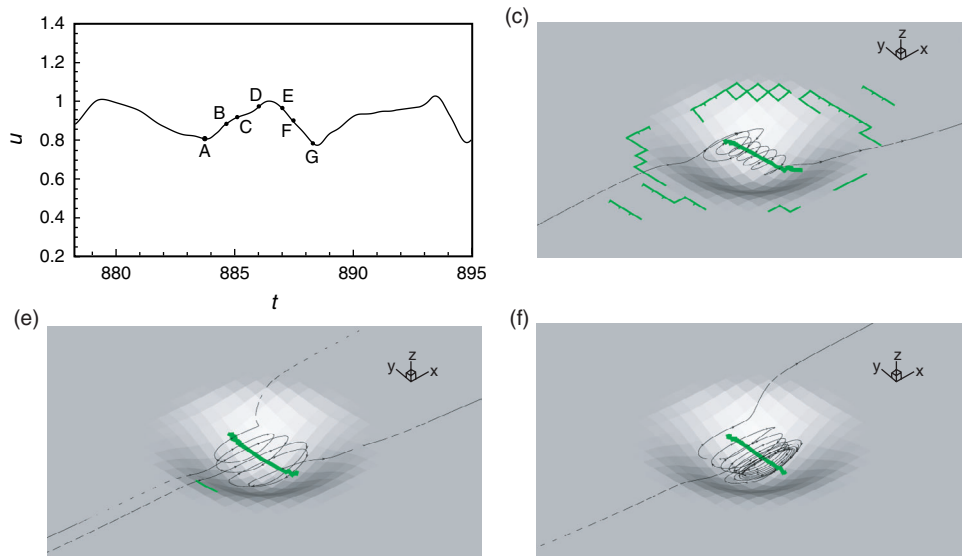


Figure 17. Streamlines and vortex cores at 7 different phases in one period corresponding to  $f = 0.20$  at  $Re = 1000$ .

the present work.

#### 4. CONCLUSION

Direct numerical simulation of the flows in a channel with a dimple at the lower wall was made at different Reynolds numbers ranging from 50 to 3000. The dimple is cosine shaped with the fixed print diameter equal to the channel half height and a depth of 0.2 print diameter. The Reynolds number effect on the flow structures and drag composition is studied.

At the Reynolds number lower than 1000, the flow keeps laminar. Arc structures are generated at the leading and trailing edge of the dimple. With the increase of the Reynolds number, the arc structures become weaker, the vortex in the dimple cavity becomes stronger and the separation region becomes bigger, resulting in the enhancement of the pressure drag.

As the Reynolds number increases beyond 1000, the flow instability is triggered, and the flow gradually becomes turbulent. In the mean flow, the arc structures generated at the rear and front edges of the dimple and inside the dimple cavity are much stronger than those in laminar flows. The strength of the vortices is enhanced when the Reynolds number increases. As the separation bubble expands in the cavity, a local high pressure drag region appears in the rear part of the dimple cavity, and causes the drastic increase in the pressure drag.

At  $Re = 1000$ , three different flow patterns are identified at three different frequencies of 0.15, 0.31 and 0.20. At the frequency of 0.15, the flow inside the cavity is characterized by an periodic erection of the spanwise vortex, at the frequency of 0.31 it is dominated by a  $\Lambda$  vortex, and at the frequency of 0.20 a relatively stable spanwise vortex survives. At even higher Reynolds numbers, the three flow pattern still exist. When the Reynolds number reaches 3000, the flow becomes fully turbulent, and the cyclinic shedding of streamwise vortices from the dimple cavity can also be observed.

#### ACKNOWLEDGEMENTS

This work is supported by National Natural Science Foundation of China (No. 10925210, 11132005).

#### REFERENCES

- [1] P.M. Ligrani, M.M. Oliveira, *Comparison of heat transfer augmentation techniques*. AIAA Journal, 2012, 41, 337–362.
- [2] P.M. Ligrani, J.L. Harrison, G.I. Mahmmod and M.L. Hill, *Flow structure due to dimple depressions on a channel surface*, Physics of Fluids, 2001, 13, 3442–3451.
- [3] G.I. Mahmood, P.M. Ligrani, *Heat transfer in a dimpled channel: combined influences of aspect*

- ratio, temperature ratio, Reynolds number, and flow structure*, International Journal of Heat and Mass Transfer, 2002, 45, 2011–2020.
- [4] S.Y. Won, Q. Zhang and P.M. Ligrania, *Comparison of flow structure above dimpled surfaces with different dimple depth in a channel*, Physics of Fluids, 2005, 17, 045105.
- [5] Z. Wang, K.S. Yeo and B.C. Khoo, *Numerical simulation of laminar channel flow over dimpled surface*, AIAA Paper, 2003, 3964.
- [6] J. Park, P.R. Desam and P.M. Ligrani, *Numerical predictions of flow structure above a dimpled surface in a channel*, Numerical Heat Transfer A, 2002, 45, 11–20.
- [7] J. Park and P.M. Ligrani, *Numerical predictions of heat transfer and fluid flow characteristics for seven different dimpled surfaces in a channel*, Numerical Heat Transfer A, 2005, 47, 209–232.
- [8] S.Y. Won and P.M. Ligrania, *Numerical predictions of flow structure and local Nusselt number ratios along and above dimpled surfaces with different dimple depths in a channel*, Numerical Heat Transfer A, 2004, 46, 549–570.
- [9] Z. Wang, K.S. YEO and B.C. KHOO, *DNS of low Reynolds number turbulent flows in dimpled channels*, Journal of Turbulence, 2006, 7, 1–31.
- [10] M.A. Elyyan and D.K. Tafti, *Large eddy simulation investigation of flow and heat transfer in a channel with dimples and protrusions*, Journal of Turbo machinery, 2008, 130, 041016-1–9.
- [11] M.A. Elyyan, A. Rozati and D.K. Tafti, *Investigation of dimpled fins for heat transfer enhancement in compact heat exchangers*, Internal Journal of Heat and Mass Transfer, 2008, 51, 2950–2966.
- [12] M.W. Ge, C.X. Xu and G.X. Cui, *Direct numerical simulation of flow in a channel with time-dependent wall geometry*, Submitted to Applied Mathematics and Mechanics.
- [13] J.D. Hudson, L. Dykhno and T.J. Hanratty, *Turbulence production in flow over a wavy wall*, Experiments in Fluids, 1996, 20, 257–265.
- [14] P. Cherukat, Y. Na, T.J. Hanratty and J.B. McLaughlin, *Direct numerical simulation of a fully developed turbulent flow over a wavy wall*, Theoretical and Computational Fluid Dynamics, 1998, 11, 109–134.
- [15] P. Chakraborty, S. Balachandar and R. J. Adrian, *On the relationships between local vortex identification schemes*, J. Fluid Mech., 2005, 535, 189–214.
- [16] S. A. Isaev, A. I. Leont'ev and P. A. Baranov, *Identification of self-organized vortexlike structures in numerically simulated turbulent flow of a viscous incompressible liquid streaming around a well on a plane*, Technical Physics Letters, 2000, 26(1), 15–18.

